

Crystallization of amorphous ceria solid solutions

Jennifer L.M. Rupp^{a,*}, C. Solenthaler^b, P. Gasser^c, U.P. Muecke^a, Ludwig J. Gauckler^a

^a Institute of Nonmetallic Inorganic Materials, Department of Materials, Swiss Federal Institute of Technology, ETH Zurich, Wolfgang-Pauli-Str. 10, CH-8093 Zurich, Switzerland

^b Laboratory for Nanometallurgy, Swiss Federal Institute of Technology, ETH Zurich, Wolfgang-Pauli-Str. 10, CH-8093 Zurich, Switzerland

^c Swiss Federal Laboratories for Materials Testing and Research, EMPA, Ueberlandstrasse 129, CH-8600 Duebendorf, Switzerland

Received 24 August 2006; received in revised form 30 January 2007; accepted 1 February 2007

Available online 28 March 2007

Abstract

Next-generation micro-solid oxide fuel cells for portable devices require nanocrystalline thin film electrolytes in order to allow fuel cell fabrication on chips at low operating temperatures and with high fuel cell power outputs. In this study amorphous gadolinia-doped ceria ($\text{Ce}_{0.8}\text{Gd}_{0.2}\text{O}_{1.9-x}$) thin film electrolytes were fabricated by spray pyrolysis and their crystallization to nanocrystalline microstructures was investigated by means of X-ray diffraction and transmission electron microscopy. At temperatures higher than 500 °C the amorphous films crystallize to a biphasic ceramic that is amorphous and nanocrystalline. The driving force for the crystallization is the reduction of the free enthalpy resulting from the transformation of amorphous into crystalline material. Self-limited grain growth kinetics prevail for the nanocrystalline grains where stable microstructures are established after short dwell times. A transition to classical curvature-driven grain growth kinetics occurs when the fully crystalline state is reached for average grain sizes larger than 140 nm and annealing temperatures higher than 1100 °C.

© 2007 Acta Materialia Inc. Published by Elsevier Ltd. All rights reserved.

Keywords: Grain growth; Crystallization; Ceramics; Ceria; Thin films

1. Introduction

Ceria-based thin films can be used as solid electrolytes in solid oxide fuel cells (SOFC) [1–5], resistive gas sensors [6–8] and catalysts. The preparation of ceria-based thin films can be performed by spray pyrolysis [9,10], spin coating [11–13], pulsed laser deposition [14], chemical vapor deposition [15] or physical vapor deposition [16]. As rather low film deposition temperatures are used in most of these preparation methods, the films are either amorphous or biphasic, exhibiting additional nanocrystalline grains (<100 nm) directly after deposition. The use of ceria-based films requires high operating temperatures above the original deposition temperature in most applications to ensure a sufficiently high electrical conductivity, gas tightness and

catalytic activity [17,18]. Therefore, the change in thermal stability, transformation of amorphous into crystalline phases, and the degree of crystallinity of these materials with respect to processing time and temperature are of prominent importance.

The grain size evolution of amorphous and dense spray pyrolyzed undoped and gadolinia-doped ceria thin films was reported in an earlier paper [19]. It was shown that the grains in these films became crystalline when heated to temperatures at or above 500 °C and that the evolution of grain size obeyed the self-limited grain growth kinetics for isothermal dwells below 1100 °C. The grains grew within the first 5–10 h of isothermal dwell until a stable microstructure at a characteristic limited grain size was established. No further grain coarsening was detected for annealing up to 30 h. The self-limited grain growth kinetics were described in accordance to Ref. [19]:

$$G - G_0 = (G_L - G_0) \left(1 - \exp^{-t/\tau_1}\right), \quad (1)$$

* Corresponding author. Tel.: +41 1 632 5651; fax: +41 1 632 1132.
E-mail address: jennifer.rupp@mat.ethz.ch (J.L.M. Rupp).

where the limited grain size G_L is the grain size reached after the relaxation time τ_1 , with the average grain size G and the initial grain size G_0 . The diffusion process in the regime of self-limited grain growth was attributed to grain boundary (interface) diffusion for nanocrystalline CGO characterized by a low activation energy of 1.32 eV.

Parallel to the self-limited grain growth, a relaxation of the microstrain in the grains was observed in these films for isothermal dwells. The microstrain of a crystalline phase reflects the ordering of atoms within the crystal lattice and the concentration of defects such as stacking faults or point defects. Material crystallizing from an amorphous state shows, at the start of crystallization, a high microstrain since the atoms are still loosely packed within the crystal lattice and defect concentration is still high. As crystallization proceeds, the microstrain decreases as the atoms order within the crystal lattice, and crystallographic density increases and defects “heal out”. The relaxation of the microstrain ε as crystallization proceeds is given over time t by an exponential decay function [19]:

$$\varepsilon = \varepsilon_L + \varepsilon_0 \exp^{-\frac{t}{\tau_2}}, \quad (2)$$

where ε_0 is a pre-exponential factor, τ_2 is the relaxation time and ε_L is the residual microstrain inside the grains after relaxation at a certain temperature. The relaxation time was found to decrease with increasing temperature for the different isothermal treatments. Microstrain and grain growth had relaxation times of the same order of magnitude, which, however, decreased with increasing temperature and as crystallization proceeded.

At temperatures higher than 1100 °C and for grains larger than 140 nm, the microstrain had fully relaxed and the material was fully crystalline. The temperature was high enough to activate volume diffusion in addition to grain boundary diffusion [20,21]. Normal grain curvature-driven growth kinetics then prevailed [22,23]:

$$G^n - G_0^n = k_n t, \quad (3)$$

where n is the grain growth exponent and k_n the characteristic material constant, which comprises the grain boundary energy and grain boundary mobility. Details of experimentally determined growth exponents [24–28] and the material constant [23] are described elsewhere. In contrast to the self-limited grain growth kinetics (Eq. (1)), the curvature-driven grain growth equation predicts unlimited grain coarsening for unlimited dwell times and is accurate for descriptions of grain growth in microcrystalline ceramics and metals.

After this grain growth study [19] it remained unclear whether the ceria-based thin films exhibiting self-limited grain growth kinetics were fully crystalline. Information about the amount of residual amorphous phase in the microstructures was not directly available from previous X-ray diffraction experiments. Especially for average grain sizes below 50 nm, it is reasonable to assume that a fraction of the material must be amorphous. If the material is not fully crystalline, i.e. consists of crystalline and amorphous

material, the self-limited grain growth kinetics might be driven by the free volumetric enthalpy change associated with the transformation of amorphous into crystalline material, similar to the transformation behavior of glass-ceramics [29]. Thus, nucleation in the amorphous phase would act in addition to pure diffusion-controlled grain coarsening, and the grain growth kinetics would differ substantially from fully crystalline ceramics or metals [30,31]. In this case, elastic strain in the amorphous phase is known to affect the Gibbs free energy of a system transforming from the amorphous to the crystalline state leading to an inhibition of the grain coarsening [32,33].

The objective of this study is to correlate the self-limited grain growth kinetics in ceria solid solutions with the microstructural evolution during the transformation of the amorphous state to the fully crystallized state. The results will contribute to the deeper understanding of grain growth kinetics in nanocrystalline ceramics and to the controlled thermal engineering of ceria-based materials for SOFC and sensor applications.

2. Experimental

Gadolinia-doped ceria, $\text{Ce}_{0.78}\text{Gd}_{0.22}\text{O}_{1.89}$, (CGO) thin films were deposited by an airblast spray pyrolysis technique on sapphire single crystals (Stettler, Switzerland). In spray pyrolysis a precursor solution is atomized to very fine droplets by air pressure. Precursor droplets hitting the heated substrate undergo pyrolytic decomposition and produce a dense and amorphous metal oxide thin film. The process is described in detail elsewhere [17,34]. For the CGO thin films a precursor solution of 0.1 mol l^{-1} was used, which contained 0.02 mol l^{-1} gadolinium chloride (Alfa Aesar, 99.9% purity) and 0.08 mol l^{-1} cerium nitrate (Alfa Aesar, 99.5% purity) in a solution of 1:1:1 vol.% ethanol, diethylene glycol monobutyl ether and methoxy propanol (all solvents from Fluka Chemie, 99.0% purity). The precursor solution was fed into the spray gun at a liquid flow rate of 34.4 ml h^{-1} and atomized by the spray gun (Compact 2000KM, Böhlföh Verfahrenstechnik, Germany) with 1 bar air pressure. The droplets produced in this manner were sprayed on a heated sapphire single crystal. This substrate was heated on a hot plate (CERAN 500, type 11A, Germany) to a temperature of $310 \pm 10 \text{ °C}$ for 3 h. Before spray deposition, the sapphire substrate temperature was directly measured on the substrate by a contact thermocouple. The orientation of the sapphire substrates was $(1\ 1\ \bar{2}\ 0)$ parallel to its surface.

A series of CGO thin films was investigated directly after deposition, after annealing at 600 and 900 °C. The films were heated and cooled at a rate of 3 °C min^{-1} without isothermal dwells.

The thermally treated CGO spray pyrolysis thin films on sapphire were sliced using the focused ion beam technique (FIB) (FEI Strata DB 235 dual beam focused ion beam workstation with integrated scanning electron microscope (SEM)) into lamellae 60–100 nm thick. These FIB lamellae

with parallel surfaces were investigated by transmission electron microscopy (TEM, Philipps CM 200 operated at 200 kV in bright-field mode with a CCD Camera Gatan).

The first step in FIB preparation was to select the area of interest of the CGO thin film by the SEM. Pt films were deposited on the selected area with an electron beam and an ion beam. These Pt films serve as protective layers for the CGO to avoid damage during FIB slicing. Stair-step trenches were milled on both sides of the Pt-deposited area with a Ga^+ ion beam of 30 kV, and the remaining material was subsequently pre-thinned to a lamella 60–100 nm thick by further Ga^+ ion beam thinning steps at low energy to remove amorphous surface layers.

For TEM the FIB lamellas were placed on carbon-coated copper grid and mounted on a single-tilt holder.

The chemical compositions of the films were verified by energy-dispersive X-ray analysis spectroscopy (EDX, LEO 1530).

Average grain size, microstrain, lattice constant and density were determined by X-ray diffraction (XRD, Bruker AXS D8 Advance). The line widths of the Bragg peaks provided information on the average grain size and on defects in the crystal lattice originating from microstrain. Lattice plane orientation was deduced from the intensity ratio between the diffraction lines of different crystal lattice directions. Diffracted X-rays from the sample were detected

by a position sensitive detector (Braun PSD ASA-S). The XRD setup was equipped with a copper radiation source ($\lambda = 0.15404$ nm) operated at 40 kV and 40 mA followed by a Ge $\text{K}\alpha_1$ monochromator (Bruker AXS). Average grain size and microstrain were determined from the full width at half maximum (FWHM) by Fourier analysis of the XRD peaks, refined by a split Pearson 7 function (Software EVA 6.0). The FWHM results from instrumental broadening, FWHM_i , and microstructure, FWHM_c . The instrumental peak broadening of the diffractometer was determined by measuring a commercially available microcrystalline and stress-free CGO powder ($\text{Ce}_{0.8}\text{Gd}_{0.2}\text{O}_{1.9-x}$ powder from Praxair, purity 99.9%). The instrumental broadening FWHM_i can be eliminated from the FWHM using the Warren and Bischoff equation [35]:

$$\text{FWHM}_c^2 = \text{FWHM}^2 - \text{FWHM}_i^2 \quad (4)$$

Average grain size and microstrain were calculated from FWHM_c according to the Scherrer and Wilson equation [36,37]:

$$\text{FWHM}_c = \frac{4K\lambda}{3\cos\theta G} + 4\varepsilon \tan\theta \quad (5)$$

The Scherrer constant $K = 0.89$ for spherical grains. λ denotes the X-ray wavelength, θ the diffraction angle, G the average grain size and ε the microstrain. Eq. (5) was

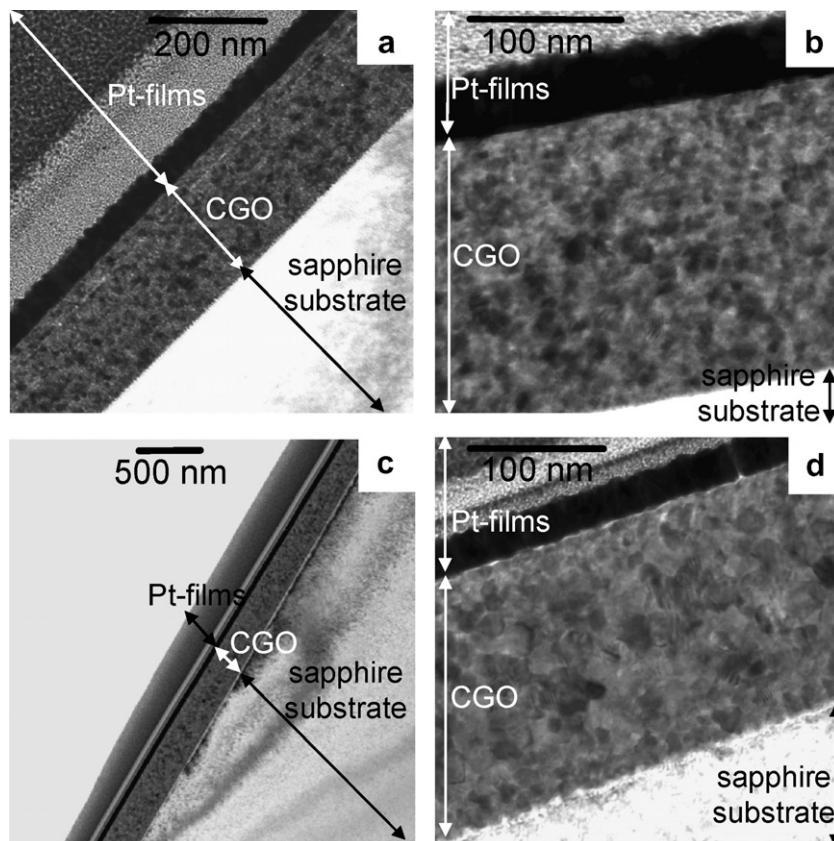


Fig. 1. TEM bright field images of spray pyrolysis deposited CGO thin films on sapphire substrates: (a, b) annealed at 600 °C and (c, d) annealed at 900 °C. The CGO thin films are all displayed in the cross-sectional view of the FIB lamella. The top Pt-films are protective layers for the FIB preparation.

evaluated by the so-called Williamson–Hall technique [38], i.e. the product $\text{FWHM}_c \cos \theta$ is plotted vs. $\sin \theta$. Average grain size and microstrain, respectively, are deduced by extracting their value from the ordinate intersection ($4K\lambda/3G$) and the slope (4ϵ).

The lattice parameter of the cubic CGO crystal lattice was calculated from the position of the observed diffraction lines in the XRD pattern, according to the following relation:

$$a = \frac{\lambda \sqrt{(h^2 + k^2 + l^2)}}{2 \sin \theta}, \quad (6)$$

where a indicates the lattice parameter of the cubic crystal lattice, and h , k and l are the Miller indices of the considered Bragg reflection. The crystallographic density was calculated by [33]:

$$\delta = \frac{Z_M}{a^3 N_L}, \quad (7)$$

where δ is the crystallographic density, Z the atomic number, M the molar mass, and N_L the Avogadro number.

3. Results and discussion

The FIB-sliced lamella of the spray pyrolysis CGO film cross-sections on sapphire substrates are shown in Fig. 1. In these micrographs grains with a globular shape without any preferred orientation are visible as well as amorphous material after spray pyrolysis deposition and crystallization by heat treatment [39]. EDX analysis revealed a chemical composition of $\text{Ce}_{0.78}\text{Gd}_{0.22}\text{O}_{1.89}$ for all CGO films investigated here.

Fig. 2 shows the XRD patterns of CGO spray pyrolysis films as deposited, annealed at 600 °C and annealed at 900 °C. The XRD pattern of the as-deposited thin film shows broad halos around the diffraction angles where distinctive peaks developed with increasing temperature and crystallization. The amorphous nature of the as-deposited spray pyrolysis film is confirmed by the XRD pattern. In the annealed films, XRD patterns revealed sharp XRD reflections according to the cubic fluorite crystal structure type of CGO [40]. The strongest peaks are the (111) and the (200) diffraction line for the 600 and 900 °C annealed films, respectively. It can be concluded that with the higher annealing temperature a preferred orientation developed with (200) lattice plane perpendicular to the sapphire surface.

Table 1 shows the calculated average grain sizes from XRD line broadening, microstrain, lattice constants and crystallographic densities for the annealed samples.

With increasing annealing temperature the thin films crystallized to average grain sizes of 11.6 and 35.4 nm as determined from the XRD patterns for 600 and 900 °C, respectively. With progressing crystallization the microstrain was reduced and the defect density reduced. The calculated average grain sizes and microstrain values agree

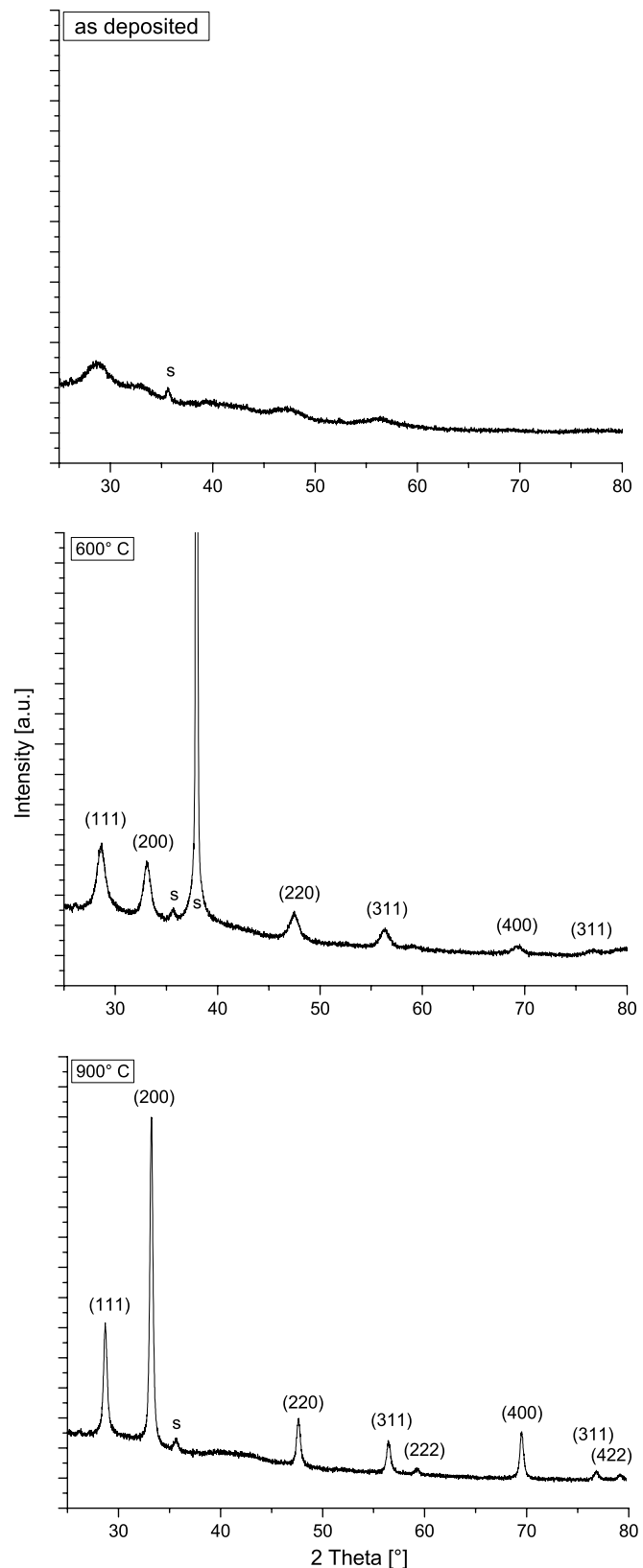


Fig. 2. XRD patterns of CGO spray pyrolysis thin film on sapphire as deposited, annealed at 600 °C and annealed at 900 °C. (The CGO peaks are designated by Miller indices and the sapphire peaks are denoted by s).

Table 1

Average grain size, microstrain, lattice constant and density for CGO spray pyrolysis thin films on sapphire annealed at 600 and 900 °C

Annealing temperature (°C)	Average grain size (nm)	Microstrain (%)	Lattice constant (nm)	Density (g/cm ³)	Reference
600	11.6	6.239	0.541	7.306	This study
800	20	1.6	0.540	7.327	[19]
900	35.4	1.522	0.538	7.372	This study

Parameters were determined from the XRD patterns.

with previously reported results on grain growth of nanocrystalline CGO spray pyrolysis films [19]. It is remarkable that with progressive crystallization (600–900 °C) the lattice constant decreases from 0.541 to 0.538 nm. This results from the increased ordering of the atoms within the crystal lattice with progressing crystallization. A consequence of the decreased lattice constant with increasing grain growth is the increase in the crystallographic density from 7.306 to 7.372 g cm⁻³.

The TEM electron diffraction patterns for the as-deposited CGO spray pyrolysis film and those annealed at 600 and 900 °C are displayed in Fig. 3. The as-deposited thin film shows no sharp rings and only broadened diffraction lines (halos). Increasing the annealing temperature led to the sharpening of these halos to defined diffraction spots and rings. These TEM observations are in accordance with the XRD patterns of the CGO films (Fig. 2).

Angle-dependent TEM imaging of the thin film cross-sections of the thermally treated films at 600 and 900 °C are presented in Figs. 4 and 5, respectively. The as-deposited materials showed no structure such as columns or pores. The annealed materials showed CGO grains and CGO grain clusters embedded in an amorphous matrix. No gradients in density of grains or grain clusters across the film thickness were observed as well as no evidence for preferred crystallization of grains at the film surface or at the film–sapphire interface.

The amorphous phase in the biphasic samples was further analyzed by tilting the specimens. Regions of the CGO thin film that did not show contrast changes during the tilt of the sample were ascribed to amorphous phases. In general, the contrast of crystalline regions showed a strong dependence on the tilt angle as the electron beam diffracts whenever a set of lattice planes is in a diffracting position. The areas of grains fulfilling the Bragg condition with respect to the tilt angle were marked with light-gray areas within a white-rimmed box of 10,000 nm² for the cross-sections of each annealed sample (Figs. 4a–f and 5a–f).

Fig. 4 shows a crystalline phase in the cross-section of the film annealed at 600 °C that changes in brightness with respect to the tilt angle and a light-gray amorphous phase that retains its gray shading independent of the tilt angle. No indications of the amorphous phase present in the microstructure were observed in the XRD patterns for the annealed samples. The average grain size determined by XRD is consistent with the average grain size revealed from the TEM micrographs.

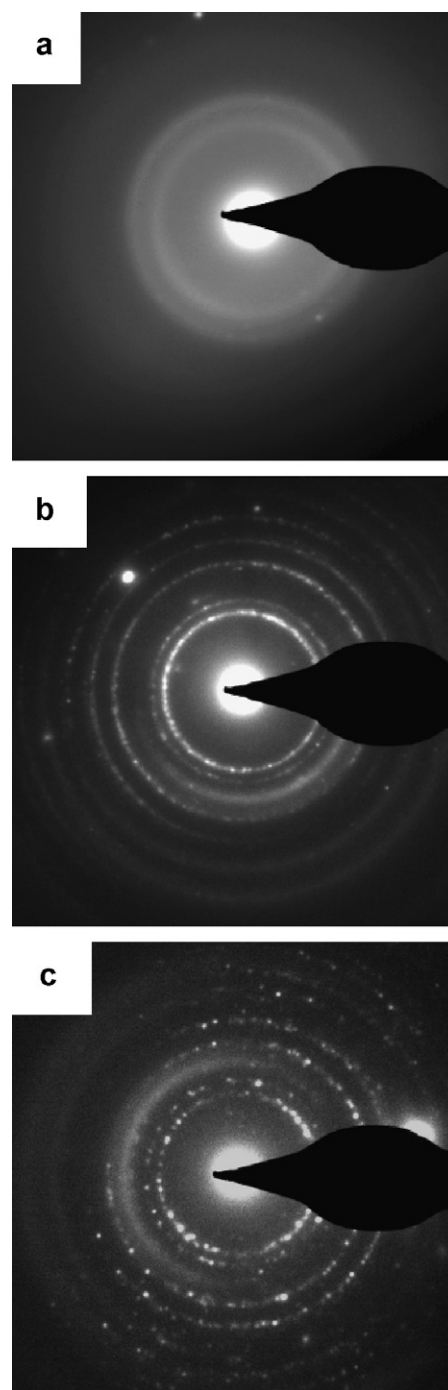


Fig. 3. Electron diffraction images of spray pyrolysis CGO thin films on sapphire: (a) amorphous CGO as deposited; (b) biphasic amorphous and crystalline CGO after annealing at 600 °C and (c) almost fully crystalline material after annealing at 900 °C.

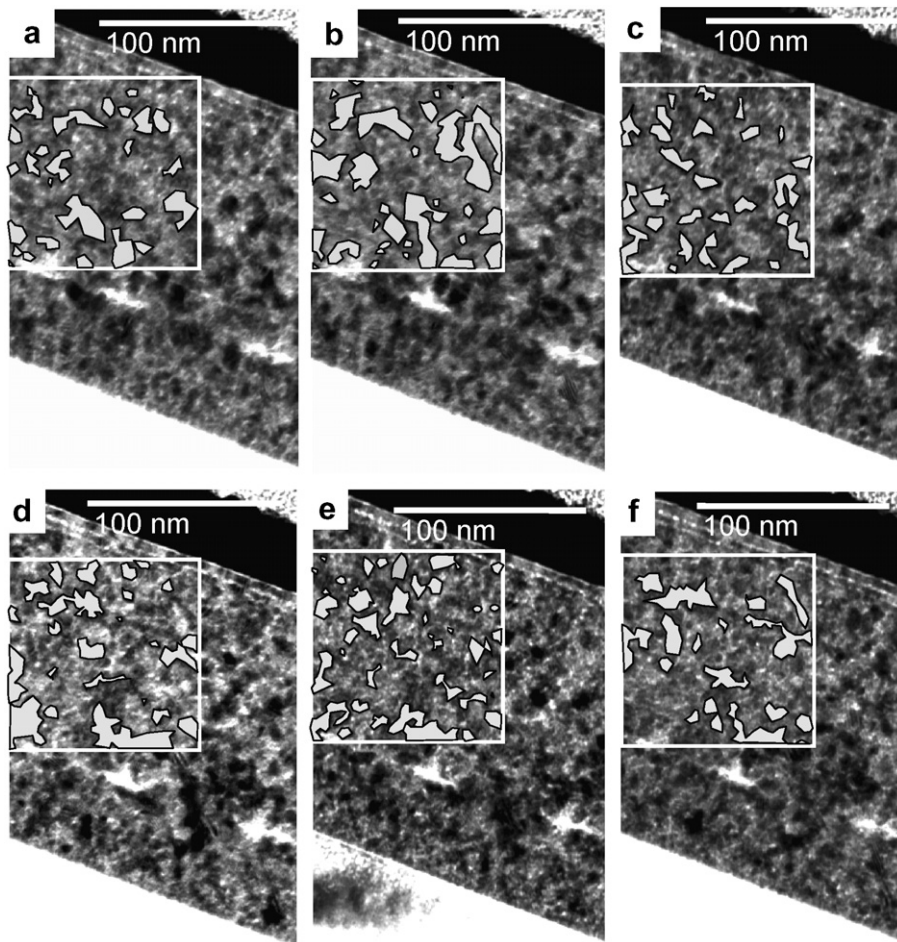


Fig. 4. Microstructure of CGO annealed at 600 °C. TEM bright field images at different tilt angles: (a) 0°; (b) 1°; (c) 2°; (d) 3°; (e) 4° and (f) 5°. Gray areas in the 10,000 nm² box change contrast and thus are identified as the crystalline phase.

The crystals of this film were assembled in clusters embedded in the amorphous surrounding matrix homogeneously throughout the cross-section. Nucleation of crystals and grain growth clearly occur simultaneously.

In Fig. 5 the cross-section of the film annealed at 900 °C is displayed with respect to the tilt angle. In contrast to the 600 °C film, this CGO thin film is better crystallized, with only sparse regions of amorphous phase. The ratio of crystalline to amorphous material increased in comparison to the specimens annealed at 600 °C and the grains appear homogeneously distributed over the cross-section. No predominant grain clustering is observed. The average grain size agrees with the average grain size given in Table 1 from the XRD measurements. The grains show typical and well-developed polygonal shapes with sharp edges and corners to their next neighbors. Amorphous phases can only be found as isolated spots between grains. As the amorphous phase is present even for this high annealing temperature, the thin films are still in a metastable equilibrium after short annealing at 900 °C.

Fig. 6 displays the superposition of the marked 10,000 nm² areas for the tilt angles studied here of the

annealed films. The gray-colored areas marked in Fig. 6 refer to the crystalline regions, while white areas indicate the amorphous regions. Since a homogeneous distribution of the grains or grain clusters is observed in the TEM projections over the film cross-sections, an even distribution can be assumed over the lamella thickness of roughly 100 nm. From these superimposed areas the ratio of crystalline to amorphous area can roughly be estimated from the marked 10,000 nm² areas for TEM lamella. Raising the annealing temperature from 600 to 900 °C leads to a decrease of amorphous phase from 31.2 ± 9 to 6.2 ± 3 vol.%.

At low temperatures (500–1100 °C) and for small grain sizes (<140 nm) the CGO was still in a state with mixed amorphous and crystallized material where grain growth and nucleation occurred simultaneously. In this region, self-limited grain growth kinetics prevail, driven by the crystallization of the amorphous phase. The crystalline material is characterized by a high microstrain and by a low crystallographic density that decreases with increasing temperature and as crystallization progresses. The contributing diffusion process for crystallization and the driving force for the transformation of amorphous material into

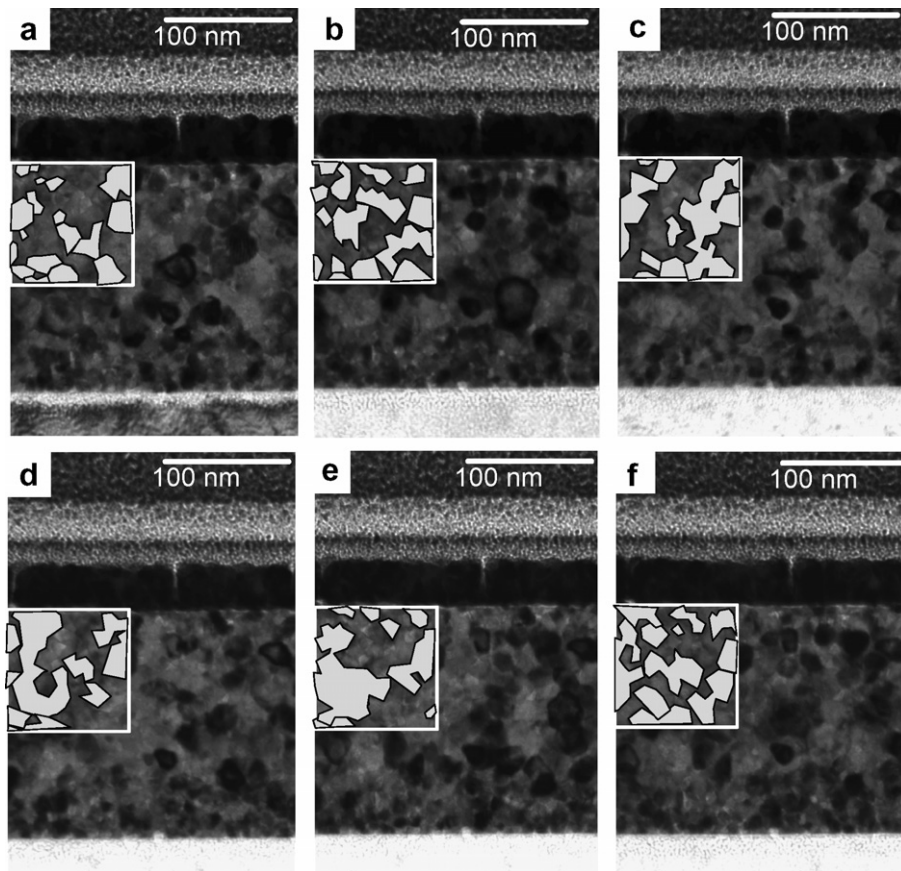


Fig. 5. Microstructure of CGO annealed at 900 °C. TEM bright field images at different tilt angles: (a) 0°; (b) 1°; (c) 2°; (d) 3°; (e) 4° and (f) 5°. Gray areas in the 10,000 nm² box change contrast and thus are identified as the crystalline phase.

crystalline within this regime of self-limited grain growth is grain boundary diffusion as reported earlier in more detail [19].

For higher temperatures and larger grains, the nanocrystalline films are fully crystalline and a transition to state-of-the-art, curvature-driven grain growth kinetics occurs. The grain growth driving force under these conditions results from grain-face intersections at nonequilibrium angles and from strong curvature at grain faces [41,42]. For fully crystalline gadolinia-doped ceria ceramics, both grain boundary and volume diffusion were previously reported to contribute to the grain coarsening [20,21].

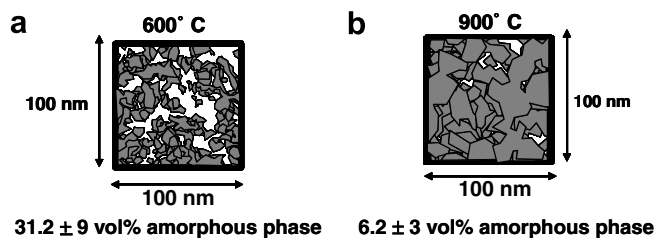


Fig. 6. Ratio of amorphous to crystalline phase determined from the tilted TEM micrographs of CGO spray pyrolysis thin films annealed at 600 and 900 °C.

4. Summary and conclusions

The spray pyrolysis process allows for the fabrication of amorphous, dense and crack-free gadolinia-doped ceria (CGO) thin films 100–400 nm thick. Temperature treatment above 500 °C leads to nucleation and grain growth within the amorphous material and CGO grains and grain clusters develop.

The driving force for the crystallization is the reduction of the free enthalpy given by the transformation of amorphous into the crystalline phase, analogous to glass-ceramics.

At low temperatures, rather stable biphasic microstructures form with clusters of crystalline grains embedded in the amorphous matrix. No preferential nucleation is observed at the surface of the thin film or at the interface with the underlying substrate.

The crystalline phase is characterized by a low crystallographic density and a high amount of microstrain inside the grains within the temperature regime of simultaneous nucleation and self-limited grain growth kinetics. Increasing crystallographic density and decreasing microstrain are observed with increasing annealing temperature (to 900 °C). Grain boundary diffusion occurs during grain coarsening and no volume diffusion is activated in this state.

At 900 °C and for short annealing times, the materials are almost fully crystalline. Microstrain inside the grains relaxes and the specific volume decreases.

At higher temperatures the normal curvature-driven grain growth kinetics apply for CGO films synthesized by spray pyrolysis, and grain growth is driven by grain-face intersections at nonequilibrium angles and by the resulting strong curvature at the grain faces.

References

- [1] Kleinogel C, Gauckler LJ. *Solid State Ionics* 2000;135:567.
- [2] Jud E, Gauckler LJ. *J Electroceram* 2005;15:159.
- [3] Skinner SJ, Kilner JA. *Mater Today* 2003;6:30.
- [4] Steele BCH. *J Power Sources* 1994;49:1.
- [5] Ormerod RM. *Chem Soc Rev* 2002;32:17.
- [6] Kosacki I, Anderson HU. *Sensor Actuat B: Chem* 1998;48:263.
- [7] Jasinski P, Suzuki T, Anderson HU. *Sensor Actuat B: Chem* 2003;95:73.
- [8] Beie H-J, Gnorich A. *Sensor Actuat B: Chem* 1991;4:393.
- [9] Taniguchi I, van Landschoot RC, Schoonman J. *Solid State Ionics* 2003;160:271.
- [10] Perednis D, Gauckler LJ. *Solid State Ionics* 2004;166:229.
- [11] Kosacki I, Suzuki T, Anderson HU, Colomban P. *Solid State Ionics* 2002;149:99.
- [12] Suzuki T, Kosacki I, Anderson HU. *Solid State Ionics* 2002;151:111.
- [13] Suzuki T, Kosacki I, Anderson HU, Colomban P. *J Am Ceram Soc* 2001;84:2007.
- [14] Coccia LG, Tyrrell GC, Kilner JA, Waller D, Chater RJ, Boyd IW. *Appl Surf Sci* 1996;96–8:795.
- [15] Choy K, Bai W, Charojrochkul S, Steele BCH. *J Power Sources* 1998;71:361.
- [16] Kleinogel C. Cathode supported thin electrolytes and nano sized ceria solid solutions for solid oxide fuel cells. PhD thesis, ETH Zurich No. 13483; 1999.
- [17] Perednis D, Wilhelm O, Pratsinis SE, Gauckler LJ. *Thin Solid Films* 2005;474:84.
- [18] Perednis D, Gauckler LJ. In: *Proceedings of the 8th international symposium on SOFCs*, 2003, Paris; 2003. p. 970.
- [19] Rupp JLM, Infortuna A, Gauckler LJ. *Acta Mater* 2005;54:1721.
- [20] Jud E, Huwiler CB, Gauckler LJ. *J Am Ceram Soc* [submitted].
- [21] Lewis GS. Low temperature sintering of solid oxide fuel cell electrolytes. PhD thesis, Imperial College of Science, Technology and Medicine, London; 2002.
- [22] Atkinson HV. *Acta Metall* 1988;36:469.
- [23] Yan MF, Cannon RM, Bowen HK. Grain boundary migration in ceramics. In: Richard M, Fulrath RM, Pask JA, editors. *Ceramic microstructures*, vol. 76. Boulder (CO): Westview Press; 1976.
- [24] Zhang TS, Ma J, Kong LB, Zeng ZQ, Hing P, Kilner JA. *Mater Sci Eng B* 2003;103:177.
- [25] Zhang T, Hing P, Huang H, Kilner J. *Mater Lett* 2002;57:507.
- [26] Malow TR, Koch CC. *Acta Mater* 1997;45:2177.
- [27] Ganapathi SK, Owen DM, Chokshi AH. *Scripta Metall Mater* 1991;25:2699.
- [28] Sagel-Ransijn CD, Winnubst AJA, Burggraaf AJ, Verweij H. *J Eur Ceram Soc* 1997;17:1133.
- [29] Jackson KA. *Kinetic processes*. Weinheim: Wiley-VCH; 2004 [chapter 15].
- [30] Rahaman MN. *Ceramic processing and sintering*. New York: Marcel Dekker; 1995. p. 642 [chapter 9].
- [31] Lu K. *Mater Sci Eng* 1996;R16:161.
- [32] Gutzow I, Schmelzer J. *The vitreous state: thermodynamics, structure, rheology, and crystallization*. Berlin: Springer; 1995. p. 302 [chapter 7].
- [33] Kleber W, Bausch H-J, Bohm J. *Einführung in die Kristallographie*; 1998. p. 200 [chapter 3, ISBN 3-341-01205-2].
- [34] Patil PS. *Mater Chem Phys* 1999;59:185.
- [35] Wagner CNJ, Aqua EN. *J Less Common Met* 1965;8:51.
- [36] Scherrer P. *Nachrichten von der Königlichen Gesellschaft der Wissenschaft zu Göttingen: Mathematisch-physikalische Klasse*; 1918. p. 1–98.
- [37] Wilson AJC. *X-ray Opt* 1949;5.
- [38] Hall W, Williamson GK. *Acta Metall* 1953;1:22.
- [39] Will J, Mitterdorfer A, Kleinogel C, Perednis D, Gauckler LJ. *Solid State Ionics* 2000;131:79.
- [40] Zhang TS, Ma J, Kong LB, Hing P, Kilner JA. *Solid State Ionics* 2004;167:191.
- [41] Burke JE, Turnbull E. *Prog Metal Phys* 1952;3:220.
- [42] Burke JE. *Trans Am Inst Min Metall Eng* 1949;180:73.